Available online at www.sciencedirect.com
ScienceDirect
International Journal of Heat and Mass Transfer 50 (2007) 3203–3215
International Journal of HEAT and MASS TRANSFER
www.elsevier.com/locate/ijhmt

Turbulent Rayleigh–Bénard convection of water in cubical cavities: A numerical and experimental study

Leonardo Valencia, Jordi Pallares *, Ildefonso Cuesta, Francesc Xavier Grau

Department of Mechanical Engineering, University Rovira i Virgili, Avinguda dels Països Catalans 26, 43007 Tarragona, Spain

Received 31 October 2005
Available online 28 March 2007

Abstract

Experimental measurements and numerical simulations of natural convection in a cubical cavity heated from below and cooled from above are reported at turbulent Rayleigh numbers using water as a convective fluid ($Pr = 6.0$). Direct numerical simulations were carried out considering the Boussinesq approximation with a second-order finite volume code ($10^7 \leqslant Ra \leqslant 10^8$). The particle image velocimetry technique was used to measure the velocity field at $Ra = 10^7$, $Ra = 7 \times 10^7$ and $Ra = 10^8$ and there was general agreement between the predicted time averaged local velocities and those experimentally measured if the heat conduction through the sidewalls was considered in the simulations.

Keywords: Natural convection; Rayleigh–Bénard flow; Partially conducting lateral walls; Numerical simulation; Particle image velocimetry turbulent flow

1. Introduction

Flows in cubical cavities have been extensively used for validation of CFD codes because of the geometrical simplicity. Despite the advantages of a numerical investigation, ultimately measurements are the only way to establish the reliability of numerical predictions. Numerical simulations of natural convection flows have been extensively performed and analyzed in the laminar and turbulent regimes. Some authors have identified different flow structures in a cubical cavity heated from below. For example, at low Rayleigh numbers, Ozoe et al. [1], predicted a single roll structure with ascending and descending flows close to two opposed lateral walls and Hernandez and Frederick [2] reported the toroidal roll which consists of four ascending currents of flow close to the vertical edges of the cavity and a single descending one along the vertical symmetry axis of the cavity. These structures and other two were reported and classified by Pallares et al. [3]. At turbulent Rayleigh numbers, Pallares et al. [4] reported the time-averaged velocity and temperature fields of large-eddy simulations of Rayleigh–Bénard convection of a Boussinesq fluid with a Prandtl number of 0.71 in a perfectly conducting cubical cavity at $Ra = 10^6$ and $Ra = 10^8$. Valencia et al. [5] studied the non-Boussinesq effects of water [6] in a cubical cavity with perfectly conducting sidewalls at $Ra = 10^7$. Leong et al. [7] measured the averaged Nusselt numbers at the cold plate of a perfectly conducting cubical cavity filled with air and with isothermal horizontal walls. These authors studied the range $10^4 \leqslant Ra \leqslant 10^8$ and three angles of inclination of the cavity but the flow topologies were not reported.

The effect of the thermal boundary conditions of natural convection flows confined by walls of finite thickness and thermal conductivity was investigated by Kim and Viskanta [8]. These authors demonstrated that the use of ideal thermal boundary conditions that neglect the interaction between the convecting fluid and the thermal conduction across the walls in numerical simulations was not a good approximation to reproduce experimental flows of air in cavities with polycarbonate lateral walls. A similar conclusion was reported by Salat et al. [9]. Ahlers [10] showed

* Corresponding author. Tel.: +34 977559682; fax: +34 977559691.
E-mail address: jordi.pallares@urv.net (J. Pallares).

0017-9310/$ - see front matter © 2007 Elsevier Ltd. All rights reserved.
doi:10.1016/j.ijheatmasstransfer.2007.01.013

Nomenclature

C	wall conductance
C_p	heat capacity (J/kg K)
d	wall thickness (m)
g	gravitational acceleration (m/s^2)
h	heat transfer coefficient (W/m^2 K)
k	thermal conductivity (W/m K)
L	dimension of the cavity (m)
N	number of grid points
Nu	Nusselt number ($Nu = hL/k$)
Pr	Prandtl number ($Pr = \nu/\alpha$)
Ra	Rayleigh number ($Ra = g\beta\Delta TL^3/\nu\alpha$)
t	time (s)
T	temperature (K)
u, v, w	velocity components (m/s)
x, y, z	Cartesian coordinates (m)

Greek symbols

α	thermal diffusivity (m^2/s)
β	thermal expansion coefficient (1/K)
δ_{ij}	Kronecker delta
Δ	increment
λ_2	second largest eigenvalue of the velocity gradient tensor
μ	dynamic viscosity (Pa s)
ν	kinematic viscosity (m^2/s)
τ	integral time scale (s)

Superscripts and subscripts

$\bar{}$	time averaged value
*	non-dimensional quantity
0	reference value at the mean temperature
C	cold plate
f	fluid
g	glass
H	hot plate
hw	horizontal walls
lw	lateral walls
t	total value of integration

that the experimental method of substraction of the conductance of the empty cell to estimate the conductance of the sidewalls could lead to errors of 20% in the Nusselt number and an important underestimation of the exponent γ of the Rayleigh number in a correlation of the form $Nu \propto Ra^{\gamma}$. The numerical results reported by Verzicco [11], who studied the effects of a sidewall with finite thermal conductivity in a cylindrical enclosure, showed that the additional heat transfer across the lateral fluid/wall interface produces an important effect on the flow and Nusselt numbers.

The objective of the present study is to compare and validate the calculated time averaged-velocity field of the turbulent Rayleigh–Bénard flow structures in a cubical cavity with partially conducting lateral walls with those measured experimentally with the particle image velocimetry (PIV) technique. The experimental setup and the numerical techniques are described in Sections 2 and 3, respectively, and the results are presented and discussed in Section 4.

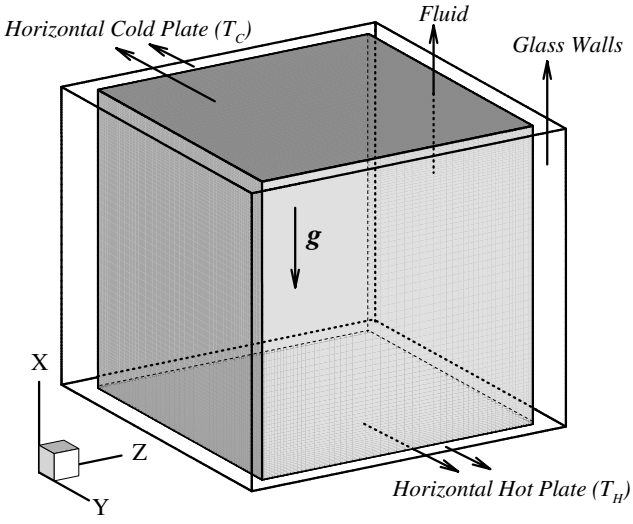

Fig. 1. Sketch showing the configuration of the cubical cell and the coordinate system.

2. Experimental

The experimental set-up used in the present work to measure the velocity field is similar to that used by Arroyo and Savirón [12] (Fig. 1). Two cubical cavities were constructed with 4-mm-thick glass lateral walls and 5-mm-thick horizontal copper plates. Table 1 shows the experimental conditions used in the experiments for the two cavities. The glass lateral walls were glued to the copper plates with Loctite 3106. The cubical cells were sandwiched between 15-mm-thick and 25-mm-thick copper blocks. Semiconductor paste was used to obtain a good thermal contact between the copper surfaces. The maximum horizontal misalignments of the cavities in the exper-

Table 1
Operating conditions of the experiments

Exp. no.	Cavity size L (m)	$\Delta T = T_C - T_H$ (°C)	T_0 (°C)	Ra_0	Pr_0
1	0.050	4.3	26.0	10^7	5.95
2	0.092	5.0	25.5	7×10^7	6.03
3	0.092	5.8	30.3	10^8	5.35

iments are estimated to be ±0.1°. The top copper block was cooled by recirculating water from a thermostatic bath and the bottom block was heated with an electrical resistance controlled by a Proportional–Integral-Derivative (PID) digital control.

Three Pt100 temperature sensors were connected and embedded in each block along its diagonal. The mean temperature of the copper blocks was calculated using the measurements of the corresponding sensors. The differences between the sensors of the same block were within ±0.02 °C. During the experiments the 15/25-mm-thick copper blocks were kept at constant temperatures within ±0.01 °C. The maximum electrical power supplied to the electric resistance was approximately 12 W. The lateral thermal boundary conditions of the experiments were fixed by the thickness and the thermal conductivity of the glass sidewalls. These conditions can be characterized by the wall conductance defined as

$$C = \frac{k_f L}{k_g d_{lw}} = \frac{1}{k^* L^*} \quad (1)$$

Eq. (1) indicates that for small thickness ($L^* \to 0$) or small thermal conductivity of the wall ($k^* \to 0$) insulation is obtained ($C \to \infty$) while values of C close to zero reveal good thermal conduction along the sidewalls that can be modeled with a constant linear temperature profile between the bottom hot wall and the cold top wall (i.e. perfectly conducting boundary conditions). Under the thermal conditions of the experiments the values of conductance are $C = 9.6$ and $C = 17.7$ for the cavities with dimensions $L = 0.05$ m and $L = 0.092$ m, respectively. These values are not as great/small to consider adiabatic/perfectly conducting walls and, consequently, the heat conduction in the glass walls has been included in the numerical simulations of the experiments.

The density of the particles used for the PIV technique with a diameter of 10 μm was slightly greater than that of the distilled water. This produced an important progressive decrease of the number of particles in the flow using water as a fluid considering the low velocities of the flow of order of several mm/s and the overall duration of some experiments of about 10 h. In order to increase the density of water, different salt solutions were tried. The most favorable results were obtained with 15 g/l of K_2SO_4 to ensure perfectly neutrally buoyant particles at T_0 and avoid chemical reactions between the salt solution and the copper plates. The variation of the physical properties of the K_2SO_4 solution with respect to the properties of water is lower than 1%.

In order to start the natural convection flow, the temperature of the cold plate was fixed at T_C, according to the conditions of the experiment (see Table 1). When T_C was reached and the value was stable, the temperature of the bottom plate was increased to T_H to obtain the desired temperature increment. Preliminary experimental tests were carried out to measure the time evolution of the velocity in two points of the cavity and typically after 30 min of constant and stable temperatures in the copper blocks the flow structure could be considered statistically developed and the image recording procedure for the PIV technique was initiated.

2.1. Particle image velocimetry

The instantaneous velocity fields were measured with the conventional PIV technique that allows the simultaneous measurement of two components of velocity in an illuminated plane of the flow. The details about this technique can be found in the review of Raffel et al. [13]. The image processing that includes the cross-correlation between two images of the fluid seeded with particles was carried out with an in-house Matlab code. The images of the full vertical section of the cavities illuminated with a laser sheet were acquired with a monochrome digital CCD camera of 480 × 420 pixels (Motion Scope PCI 1000 S) running at 10 frames per second to obtain maximum particle displacements of about 0.8 mm (3–6 pixels) between two consecutive images. The images were acquired during periods of approximately of 10 s. After this period the images were saved from the video memory of the camera to the computer disk and another acquisition period was started. This continuous process was carried out during 30 min approximately at $Ra = 10^7$. At $Ra = 7 \times 10^7$ and $Ra = 10^8$, periods of about 13 and 9 h of acquisition process were required because of the large wavelengths present in the time evolution of the flow at these Rayleigh numbers. The images of the vertical cross-section of the cavities were divided into 27 × 27 overlapped interrogation windows of 30 × 30 pixels (3.57 × 3.57 mm for the cavity with $L = 0.05$ m and 6.57 × 6.57 mm for that with $L = 0.092$ m). The maximum errors of the PIV technique used to measure the local instantaneous velocity components were estimated to be about 7%. This value was obtained by analyzing synthetic particle images generated with numerically simulated instantaneous velocity fields. A complete description of the determination of this error can be found in Valencia [14].

3. Numerical method

The physical model consists in a cubical cavity full of water ($Pr = 6.0$) with rigid lateral glass walls of thickness $d_{lw} = 0.004$ m and thermal conductivity $k_g = 0.78$ W/m °C. A sketch of the cell and the coordinate system adopted is shown in Fig. 1. The two horizontal walls are considered isothermal. Radiation heat transfer, compressibility effects and viscous dissipation are neglected. Table 2 shows the relevant physical properties of the fluid and the maximum variation of physical properties between the cold and the hot temperatures for the present simulations and experiments. It can be seen that the maximum variation is only 18% for β at $Ra = 7 \times 10^7$. According to previous studies [5] at $Ra = 10^7$ and $Pr = 5.9$, the differences in the flow structure and in the averaged Nusselt

Table 2
Values of the physical properties at the mean temperature and their variation with temperature expressed as $(\%n = (n_{T_H} - n_{T_C}) * 100/n_{T_0})$

Ra	β_0 [15]	$\%\beta$	μ_0 [16]	$\%\mu$	k_0 [17]	$\%k$	C_{p0} [17]	$\%C_p$	ρ_0 [17]	$\%\rho$
10^7	2.64×10^{-4}	15.4	8.7×10^{-4}	9.7	0.61	1.2	4160	0.14	996.2	0.10
3×10^7	2.61×10^{-4}	7.6	8.8×10^{-4}	4.7	0.61	0.6	4157	0.07	996.3	0.05
5×10^7	2.61×10^{-4}	12.6	8.8×10^{-4}	7.9	0.61	1.0	4157	0.11	996.3	0.08
7×10^7	2.59×10^{-4}	18.0	8.8×10^{-4}	11.2	0.61	1.4	4160	0.16	996.4	0.11
10^8	3.04×10^{-4}	17.5	8.0×10^{-4}	12.1	0.62	1.5	4163	0.17	995.2	0.14

numbers are not significant between a simulation considering the Boussinesq approximation and a simulation carried out considering the variation of 62%/40% in β/μ between the temperatures of the cold and hot plates. Consequently, the Boussinesq approximation has been adopted in the present simulations. For the simulations at $Ra = 10^7$, $Ra = 7 \times 10^7$ and $Ra = 10^8$ the experimental conditions shown in Table 1 were adopted.

The governing dimensionless equations in Cartesian coordinates, considering a Boussinesq fluid, are

the continuity equation:

$$\frac{\partial u_i^*}{\partial x_i^*} = 0 \tag{2}$$

the momentum equations:

$$\frac{\partial u_i^*}{\partial t^*} + \frac{\partial (u_j^* u_i^*)}{\partial x_j^*} = -\frac{\partial p^*}{\partial x_i^*} + Pr_0 \frac{\partial^2 u_i^*}{\partial x_j^{*2}} + Ra_0 Pr_0 T^* \delta_{i1} \tag{3}$$

the thermal energy equation:

$$\frac{\partial T^*}{\partial t^*} + \frac{\partial (u_i^* T^*)}{\partial x_i^*} = \frac{\partial^2 T^*}{\partial x_i^{*2}} \tag{4}$$

and the thermal energy equation for the walls:

$$\frac{\partial T^*}{\partial t^*} = \alpha^* \frac{\partial^2 T^*}{\partial x_i^{*2}} \tag{5}$$

In Eq. (5), $\alpha^* = \alpha_g/\alpha_f$, is the ratio between thermal diffusivity of the glass and thermal diffusivity of water ($\alpha_g = 3.4 \times 10^{-7}$ m^2/s and $\alpha_f = 1.4 \times 10^{-7}$ m^2/s) [17]. The scales used for length, velocity, time and pressure are L, α_0/L, L^2/α_0 and $\alpha_0^2 \rho_0/L^2$, respectively. The non-dimensional temperature is defined as $T^* = (T - T_0)/\Delta T$ where $\Delta T = (T_H - T_C)$ and T_0 is the mean temperature $T_0 = (T_H + T_C)/2$. The six walls are assumed to be rigid and static ($u_i^* = 0$) and the thermal boundary conditions at the hot and cold plates are $T_H^* = 0.5$ and $T_C^* = -0.5$, respectively. The lateral thermal boundary conditions for the fluid are fixed by the dimension and the material of the lateral vertical walls of the cavities used in the experiments. The physical properties of the glass at 20 °C relevant for the simulations are $k_g = 0.78$ W/m °C, $C_{pg} = 840$ J/kg °C and $\rho_g = 2700$ kg/m^3 [17]. The Rayleigh numbers of the air around the cavities based on the height and the maximum temperature difference of the cavities are 4×10^7, 3×10^8 and 3.3×10^8 for the experiments 1, 2 and 3, respectively (Table 1). In order to set the boundary condition on the outer surface of the lateral walls the heat transfer coefficient of the outer surface of the lateral walls was calculated considering a typical heat transfer coefficient for a vertical plate and $Ra < 10^9$, $h = 1.42[(T_{lw} - T_0)/L]^{1/4}$ [17], where T_{lw} is the temperature of the external surface of the wall and L is the vertical dimension of the plate. The lateral heat loses predicted are only 1.0% of the heat conduction transferred across the lateral walls from the hot to the cold plate and the heat transfer between the horizontal walls and the convecting fluid. Consequently, in the simulations, a perfectly adiabatic boundary condition was imposed at the outer surface of the sidewalls.

Eqs. (2)–(5) and the corresponding boundary conditions have been solved numerically with the CFD control volume code 3DINAMICS. In this second-order accuracy code, the diffusive and convective fluxes are discretized in a staggered grid using a central scheme. The code performs the time-marching procedure with an explicit Adams–Bashforth scheme. The coupling between the pressure and velocity field is computed with the predictor-corrector scheme, which involves the numerical solution of a Poisson equation with a conjugate gradient method. The details of the complete mathematical formulation and the description of the numerical methods can be found in Cuesta [18]. Numerical simulations at the Rayleigh numbers considered in this study, were conducted with non-uniform grids of $N_x = 81$, $N_y = 61$ and $N_z = 61$ nodes and the heat transfer across the lateral walls was calculated using 8 additional nodes in the perpendicular direction of each wall at $Ra = 10^7$, $Ra = 3 \times 10^7$ and $Ra = 5 \times 10^7$ and 5 additional nodes at $Ra = 7 \times 10^7$ and $Ra = 10^8$. Table 3 shows the minimum and maximum grid spacing of the mesh used in the numerical simulations. The time steps used range from $\Delta t^* = 2 \times 10^{-7}$ at $Ra = 10^8$ to $\Delta t^* = 5 \times 10^{-7}$ at $Ra = 10^7$.

Large-eddy simulations at $Ra = 10^8$ and $Pr_0 = 6$ were initially carried out with the dynamically localized subgrid scale (SGS) model used by Pallares et al. [4] to check the subgrid scale contribution for the computational conditions of the present study. It was found that at $Pr_0 = 6$, the maximum time-averaged ratios between the local sub-

Table 3
Minimum and maximum grid spacing of the mesh used in the numerical simulations at $Pr = 6.0$ and at Rayleigh numbers 10^7, 3×10^7, 5×10^7, 7×10^7 and 10^8

N_x	N_y	N_z	Δx^*_{min}	Δx^*_{max}	$\Delta y^*_{min} = \Delta z^*_{min}$	$\Delta y^*_{max} = \Delta z^*_{max}$
81	61	61	0.004	0.028	0.008	0.030

grid-scale viscosity and the molecular viscosity in the cavity were only 0.1% with a standard deviation of 0.2%. These small contributions agree with those reported by Pallares et al. [4] at lower Prandtl number ($Pr = 0.7$). The grid resolution used has at least 3 grid nodes within the time-average thermal boundary layers near the horizontal walls at the highest Rayleigh number studied ($Ra = 10^8$).

4. Results and discussion

In this section the numerical results of the time-averaged flow structures and the averaged Nusselt numbers at the horizontal cold plate are reported for $Ra = 10^7$, $Ra = 3 \times 10^7$, $Ra = 5 \times 10^7$, $Ra = 7 \times 10^7$ and $Ra = 10^8$. The measured and numerically predicted time-averaged velocity field on a vertical mid-plane of the cavity are compared at Rayleigh numbers $Ra = 10^7$, $Ra = 7 \times 10^7$ and $Ra = 10^8$. As initial conditions for the simulations, the instantaneous velocity and thermal field at $Ra = 10^7$ and $Pr = 5.9$ in a cavity with perfectly conducting lateral walls computed by Valencia et al. [5] was used. The results at higher Rayleigh numbers were obtained from instantaneous flow fields using a step change of the Ra number.

4.1. Numerical and experimental results at Rayleigh number 10^7

The time averaged flow structure obtained numerically at $Ra = 10^7$ is shown in Fig. 2 in terms of isosurfaces of the second largest eigenvalue of the velocity gradient tensor following the method to detect the occurrence of vortex cores proposed by Jeong and Hussein [19] (Fig. 2a) and in terms of two isosurfaces of the vertical velocity component (Fig. 2b). The averaged flow and temperature fields and the flow statistics at $Ra = 10^7$ were obtained by sampling the statistically developed velocity and thermal fields during $t_t^* = 1.61$ non-dimensional time units ($t_t = 456$ min of dimensional time considering a cavity of $L = 0.05$ m). This sampling period was started after $t_t^* = 0.7$ from the initial conditions. The time averaged flow topology at this Rayleigh number can also be seen in Fig. 3 in terms of the velocity vectors field on the vertical mid-planes ($z^* = 0.5$ and $y^* = 0.5$) of the cavity. The averaged flow structure at $Ra = 10^7$, which is very similar to that reported by Valencia et al. [5] at the same Rayleigh number for a cavity with perfectly conducting lateral walls, consists in two main counter rotating vortex rings located near the horizontal walls and eight small vortex tubes near the vertices of the cavity, as shown in Fig. 2. The vortex rings can be understood as a combination of four z-rolls (with vorticity aligned with the z-direction) and four y-rolls (with vorticity aligned with the y-direction), as shown in Fig. 3a and b. It can be seen that the time-averaged topology is symmetric with respect to the horizontal and vertical mid-planes of the cavity.

The numerically predicted and the experimentally measured cross section of the y-rolls are shown in Fig. 3b and c, respectively. These figures show that there is a general agreement between the calculated and the measured velocity fields and the fluctuation intensities of the vertical velocity (u). It can be seen that, in general, the fluctuation intensities predicted numerically are greater than those measured experimentally. As reported by Lecordier et al. [20] a reduction of a 5% of the fluctuation intensities can be attributed to the filtering effect of the relatively large interrogation windows. The present results, obtained with interrogation windows of 30×30 pixels, show maximum differences of the fluctuation intensities between the measurements and the simulation of about 10% (see, for example, Fig. 3b and c).

The first five rows of Table 4 show the values of the integral scale and the number of integral scales sampled (t_t^*/τ^*), at $Ra = 10^7$, of the surface averaged Nusselt number on the cold plate (Nu_C) and u^*, v^* and T^* at the position $x^* = 0.5$,

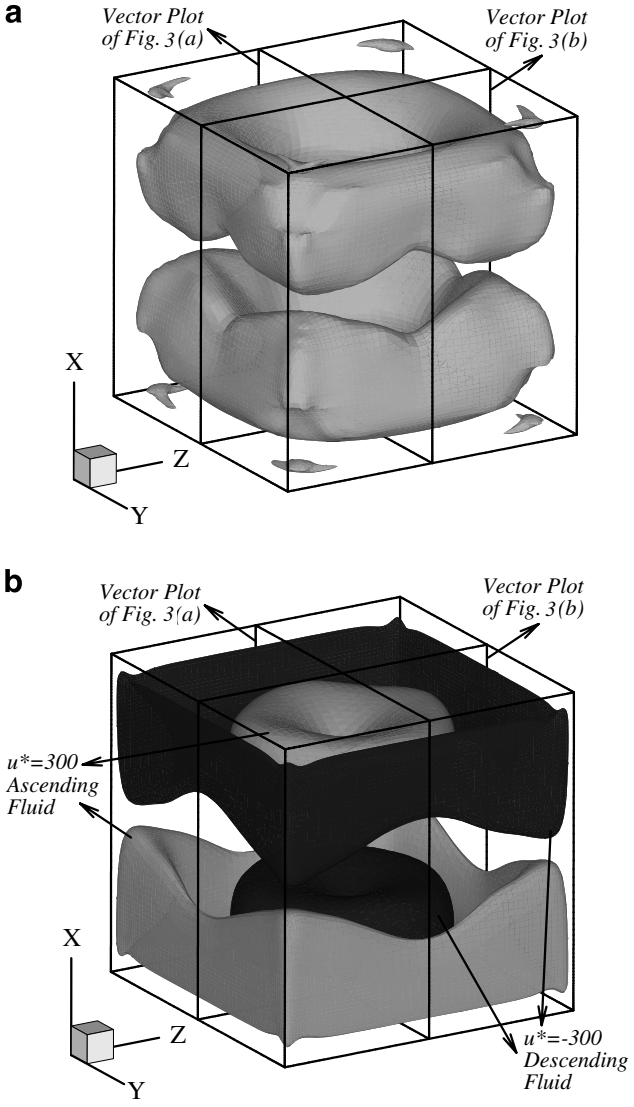

Fig. 2. Time averaged flow fields at $Ra = 10^7$ for a total integration time of $t_t^* = 1.61$ (7.6 h). (a) Surface of constant value of $\lambda_2/|\lambda_{2,\max}| = -0.02$. (b) Isosurfaces of the vertical velocity component, $u^* = \pm 300$.

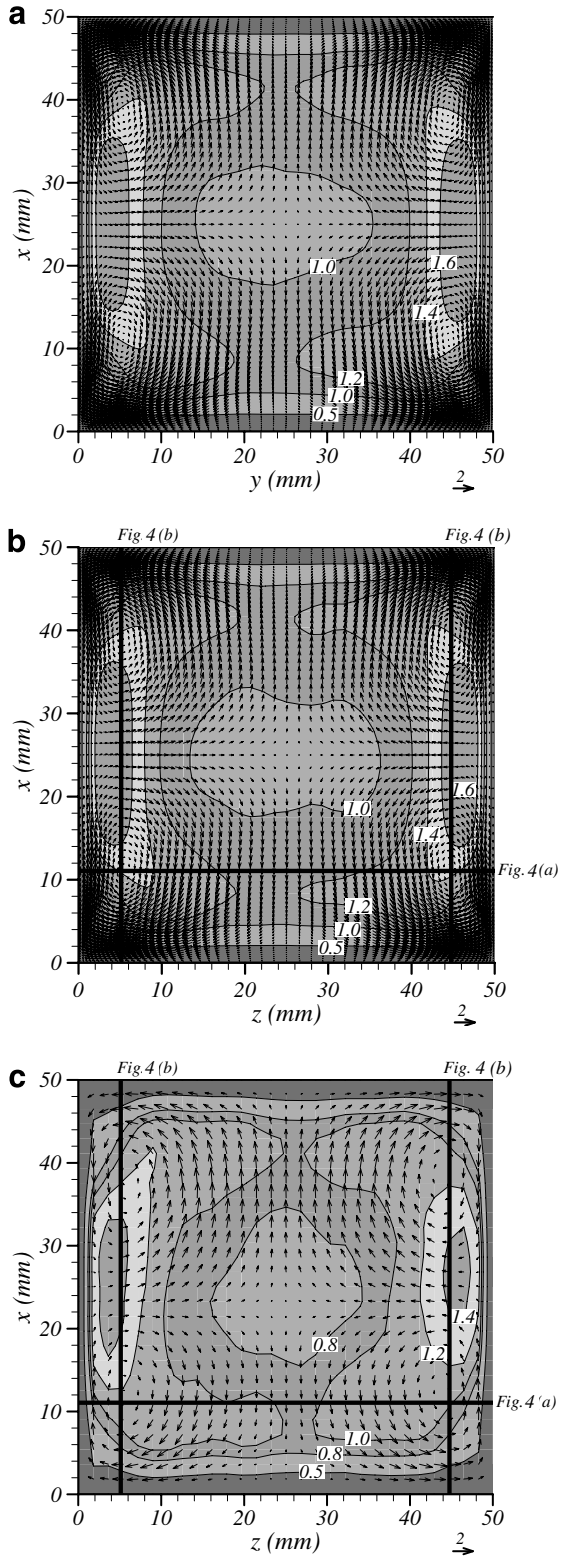

Fig. 3. Velocity fields and RMS values of u at $Ra = 10^7$ on the vertical mid-planes. (a) and (b) numerical fields at $z = 25$ mm and $y = 25$ mm, respectively, (c) experimental velocity field at $y = 25$ mm. These planes are indicated in Fig. 2a and b. The reference vectors are depicted near the bottom right corner of each vector plot.

$y^* = 0.75$ and $z^* = 0.5$. It can be seen that the total integration time, at this Rayleigh number, ranges from 191 to 2920 times the integral scale and consequently the number of data taken is adequate to calculate the time averaged values.

Table 4
Integral scale (τ^*), number of integral scales sampled (t_t^*/τ^*) and statistical quantities for the averaged Nusselt number at the cold plate (Nu_C), and for u^*, v^* and T^* at the point $x^* = 0.5$, $y^* = 0.75$ and $z^* = 0.5$

	Integral scale (τ^*)	(t_t^*/τ^*)	Mean value ($\overline{n^*}$)	RMS
$Ra = 10^7$ ($t_t^* = 1.61$)				
Nu_C	6.2×10^{-4}	2595	16.6	0.76
u^*	8.3×10^{-3}	195	25.0	466.1
v^*	4.9×10^{-3}	331	−226.6	233.9
T^*	8.5×10^{-3}	191	-1.3×10^{-4}	0.04
$Ra = 3 \times 10^7$ ($t_t^* = 0.85$)				
Nu_C	4.1×10^{-4}	2066	25.1	0.95
u^*	6.5×10^{-2}	13	365.8	926.4
v^*	3.1×10^{-3}	274	−207.2	470.4
T^*	2.5×10^{-2}	35	3.8×10^{-3}	0.03
$Ra = 5 \times 10^7$ ($t_t^* = 0.75$)				
Nu_C	1.2×10^{-3}	636	30.7	1.05
u^*	1.9×10^{-1}	4	−511.2	1147.9
v^*	2.6×10^{-3}	285	−264.17	610.4
T^*	3.5×10^{-2}	21	-4.5×10^{-3}	0.025
$Ra = 7 \times 10^7$ ($t_t^* = 0.86$)				
Nu_C	1.4×10^{-3}	631	35.0	1.15
u^*	9.7×10^{-2}	9	121.4	1513.8
v^*	7.7×10^{-4}	1111	−266.9	734.2
T^*	7.9×10^{-2}	11	5.5×10^{-4}	0.024
$Ra = 10^8$ ($t_t^* = 0.56$)				
Nu_C	2.0×10^{-4}	2822	40.4	1.19
u^*	8.1×10^{-2}	7	−645.0	1429.5
v^*	5.0×10^{-4}	1116	−329.2	831.5
T^*	1.2×10^{-2}	47	-4.1×10^{-3}	0.022

At the Rayleigh numbers studied the flow shows large fluctuations in the velocity and temperature fields with respect to the time averaged values as can be deduced comparing the time averaged values of the velocity with their corresponding fluctuation intensities, shown in Fig. 3. It can be seen that the RMS values are significantly larger than the time averaged values near the horizontal midplane of the cavity indicating an intensive turbulent transfer near this region. The mean value and the standard deviation of the averaged Nusselt number at the cold plate at $Ra = 10^7$ are very similar to those reported by Valencia et al. [5] at the same Rayleigh number with perfectly conducting lateral walls. The mean value/standard deviation is only 1.3%/4.2% smaller/larger for the present study.

Fig. 4a and b show the numerical and experimental time-averaged velocity profiles along the lines indicated in Fig. 3b and c. The maximum differences between the experimental and the numerical vertical velocities can be observed close to the walls (see for example Fig. 4b). This difference can be attributed to the finite size of the interrogation volumes used in the PIV technique when the velocity is measured in regions with large velocity gradients.

The vertical velocity profile of the time averaged flow structure in a perfectly conducting cavity at $Ra = 10^7$

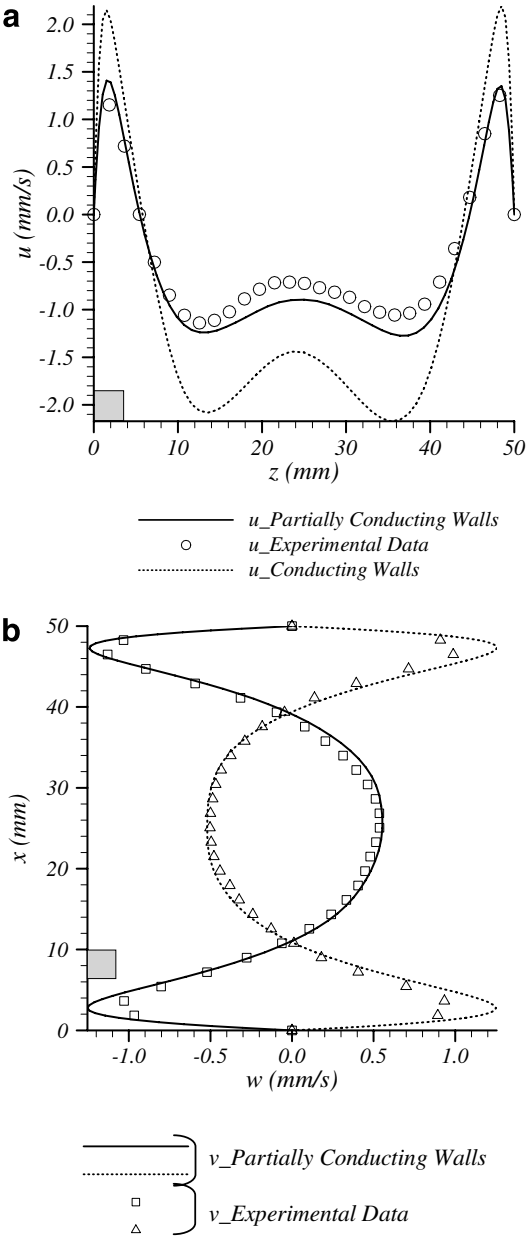

Fig. 4. Velocity profiles obtained from the simulations and from the measurements of the time averaged flow topology at $Ra = 10^7$. These profiles are indicated in Fig. 3b and c. (a) Horizontal (y) profiles of the vertical velocity component (u), along the line $x = 11.1$ mm, $z = 25$ mm ($z^* = 0.5$). (b) vertical (x) profiles of the horizontal velocity component (v) along the lines $y = 4.7$ mm, $z = 25$ mm and $y = 45.2$ mm, $z = 25$ mm. The gray squares indicate the size of the interrogation window used in the experiments.

reported by Valencia et al. [5] is also included in Fig. 4a for comparison. It can be seen that close to $z = 37$ mm velocities are about 110% larger for the perfectly conducting cavity indicating that the effect of the thermal conductivity of the walls is important in the simulations to reproduce the experimental measurements. Although the averaged Nusselt number at the horizontal walls in the present study are very similar to those calculated with perfectly conducting walls, the volume averaged modulus of the velocity vector is 290 non-dimensional velocity units. This value is 36% smaller for the simulation considering the finite value of the wall thermal conductivity in comparison with the value reported by Valencia et al. [5] in a perfectly conducting cavity. This reduction of the velocities, also shown in Fig. 4a, can be explained with the help of Fig. 5c. This figure shows the vertical profile ($y^* = 1.041$) of the temperature inside the wall of the cavity on the mid-plane $z^* = 0.5$, for the simulations with perfectly conducting walls and for the simulations considering finite thermal conductivity of the lateral walls. Fig. 5c reveals that in the lower region of the cavity ($x^* < 0.5$), the temperatures for the perfectly conducting lateral walls are larger than those corresponding to simulations with partially conducting walls. These larger values of temperature produce an overall increase of the buoyancy term in the vertical momentum equation in these regions and, consequently, an increase of the magnitude of the vertical velocities.

Fig. 5a shows time averaged temperature contours of the fluid close to the glass walls on the vertical planes $y^* = 0.996$ and $z^* = 0.004$ at $Ra = 10^7$. It can be seen that the departure from the linear velocity profile of the perfectly conducting conditions is found along all the area of the lateral walls. The temperature contours on the vertical mid-plane indicated in Fig. 5a are depicted in Fig. 5b. This figure shows that more of the 90% of the volume of the fluid is between the range $T^* = -0.1$ and $T^* = 0.1$ according to the fact that $Pr > 1$ and because of the good mixing produced by the mean flow and the turbulence intensities, that restricts the temperature gradients to the thin thermal boundary layers near the horizontal walls of the cavity. The temperature contours in the lateral walls shown in Fig. 5b indicate that the heat transfer in the walls is not only from the hot to the cold plates; it can be seen that the heat is also transferred from the fluid to the walls in the lower part of the cavity and from the walls to the fluid close to the top of the cavity.

4.2. Time evolution of the flow structure at $Ra = 3 \times 10^7$, $Ra = 5 \times 10^7$, $Ra = 7 \times 10^7$ and $Ra = 10^8$

This section describes the time evolution of the average flow structure and the averaged Nusselt number at the cold plate at $Ra = 3 \times 10^7$, 5×10^7, 7×10^7 and 10^8. Because of the similitude of the time averaged flow structures found in the range $3 \times 10^7 \leqslant Ra \leqslant 10^8$, the discussion is centered in the experimental flow topology measured at $Ra = 7 \times 10^7$.

Fig. 6b shows the time evolution of the instantaneous vertical velocity component (u^*) at $Ra = 7 \times 10^7$ at the position $x^* = 0.5$, $y^* = 0.75$ and $z^* = 0.5$. This position inside the cavity is indicated in Fig. 6a and c. The time evolution of the vertical velocity component shown in Fig. 6b has very low frequencies superimposed to a range of higher frequencies. It can be seen that the low frequencies produce large periods of time of positive instantaneous values (for example between 0.1 and 0.25 non-dimensional units of time)

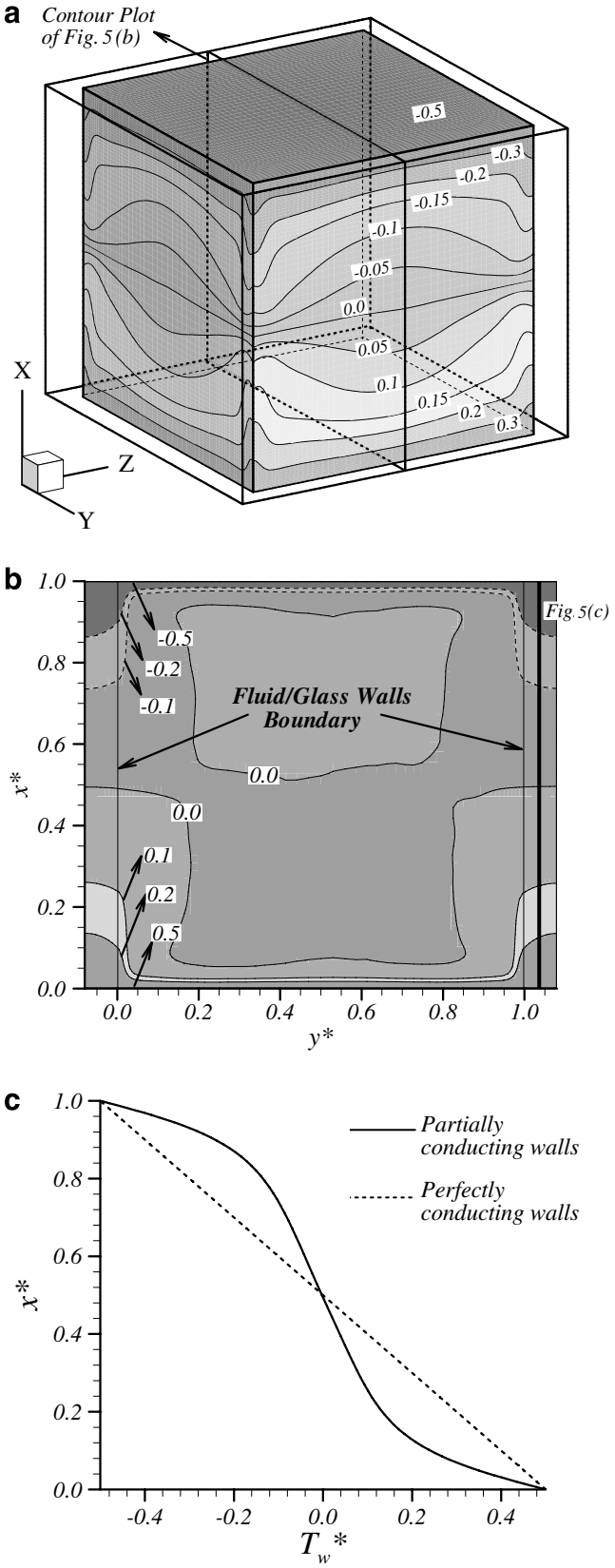

Fig. 5. (a) Temperature contours of the time averaged temperature field of the fluid close to the glass walls at $Ra = 10^7$, (b) temperature contours on the vertical mid-plane, (c) temperature profile indicated in figure (b) for the simulations with perfectly conducting walls and considering the finite conductivity of the lateral walls.

followed by periods in which the values are negative (for example between 0.3 and 0.5 non-dimensional units of time). The different time averaged flow fields obtained by averaging the instantaneous flow during the periods of time corresponding to the low frequencies have been identified as four different flow configurations that are denoted as (A), (B), (C) and (D). It can be considered that the low frequency time evolution corresponds to the periodic oscillation of the flow between these four basic flow configurations.

These four averaged flow configurations were obtained by averaging the velocity flow field during different periods of time. Each period of time could contain from 0.03 to 0.16 non-dimensional time units. The four possible configurations of the average flow structure obtained at $Ra = 7 \times 10^7$ are depicted in Fig. 6c in terms of the vertical velocity contours on the horizontal mid-plane $x^* = 0.5$. The period of time in which each configuration occurs in the time evolution of the vertical velocity of the analyzed point is indicated above the horizontal axis of Fig. 6b.

The averaged flow structure of each configuration consists in two main descending and ascending flows that occur close to two diagonally opposed vertical edges similar to the laminar flow topology named S2 in previous studies [3]. Fig. 7 shows the averaged flow structure in terms of isosurfaces of two values of the vertical velocity for configuration (C) (i.e. ascending fluid near the corner $y = 92$ mm, $z = 0$ mm and descending fluid near $y = 0$ mm, $z = 92$ mm). The time averaged flow topology of this configuration can also be seen in Fig. 8 in terms of the velocity vectors field on the vertical mid-planes ($z^* = 0.5$ and $y^* = 0.5$) of the cavity (see Fig. 8a and b). It can be seen that this combination of main ascending and descending flows is associated with a single rolling motion with its axis of rotation horizontally oriented and perpendicular to two diagonally opposed vertical edges of the cavity. Fig. 6c shows that the main difference between the flow configurations or positions of the flow topology is the diagonally opposed pair of corners used by the fluid to ascend from the hot plate and descend from the cold plate. For example, Fig. 6b indicates that the positive mean vertical velocities at the position $x^* = 0.5$, $y^* = 0.75$ and $z^* = 0.5$ are found in configurations (C) and (D) and the negative mean vertical velocities occur in configurations (A) and (B). The change of the sign of the instantaneous vertical velocity plotted in Fig. 6b agrees with the changes of the configuration of the structure. The changes from positive to negative velocity values indicate that the mean flow structure evolves from (A) to (D) or from (B) to (C) and the changes from negative to positive values, correspond to the inverse evolutions. This change of flow configuration, which has associated a very low frequency, can be understood as a progressive rotation on the horizontal plane of the rotation axis of the single roll flow structure. It can be seen in Fig. 6b that this rotation of the roll axis, or of the overall flow structure, around the vertical axis of the cavity that produces the evolution between two flow configurations can be clockwise (i.e. from (A) to (D)) or

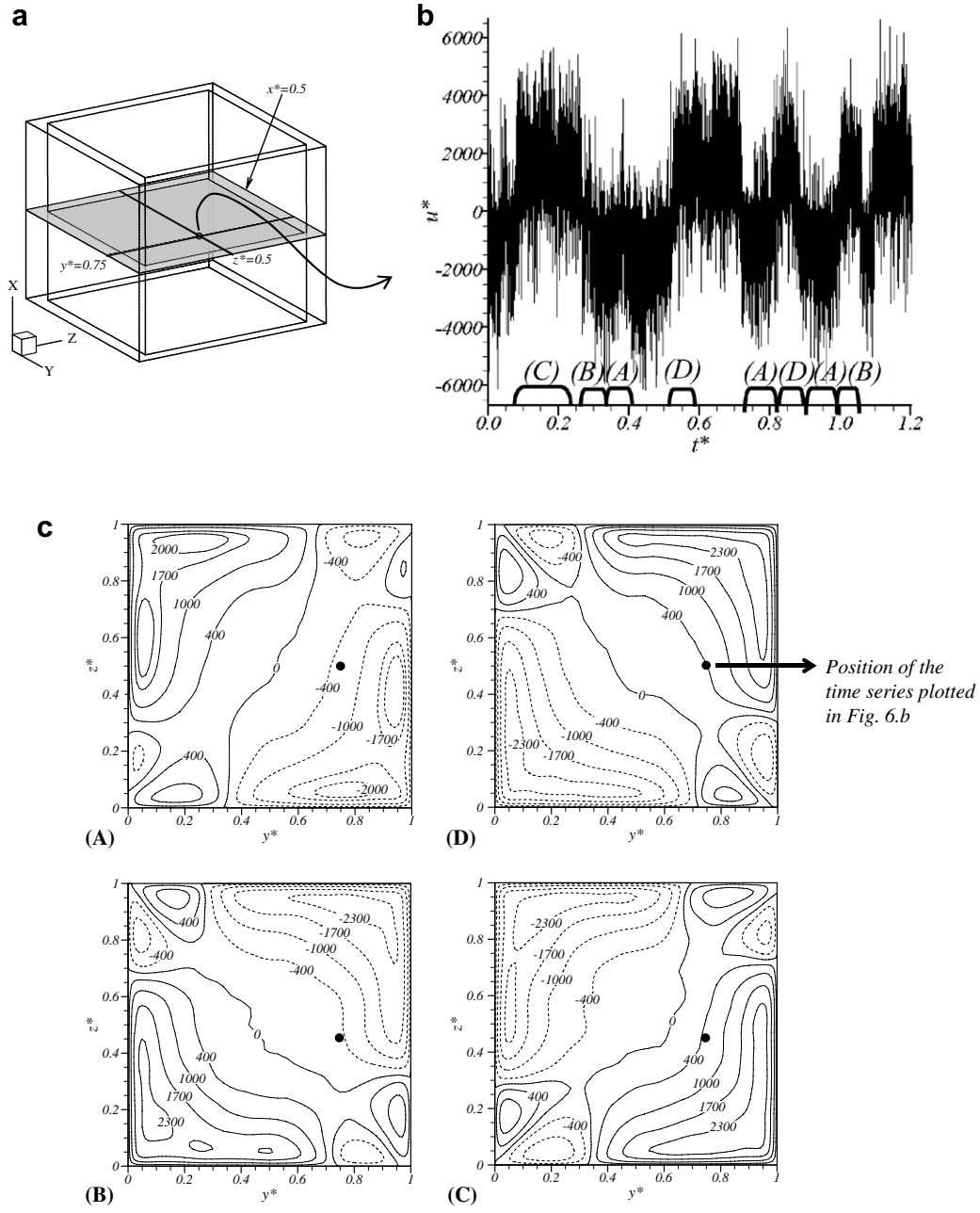

Fig. 6. (a) Sketch of the position of the point used in the analysis of the time evolution of some variables (see figure (b) and Table 4), (b) time evolution of the vertical velocity component (u^*) at the position indicated in figure (a), the letters (A), (B), (C) or (D) near the x-axis indicate the configuration (see figure (c)) of the flow structure in the period of time showed by the parenthesis. (c) Contours of the vertical velocity (u^*) on the horizontal mid-plane for the four configurations of the structure at $Ra = 7 \times 10^7$. Continuous/dashed line contours correspond to positive/negative values. The black point indicates the position depicted in figure (a).

anticlockwise (i.e. from (A) to (B)). It should be noted that the direct transition from (A) to (C), (C) to (A), (B) to (D) or (D) to (B) are not possible, and in fact have not observed, according to the rotation of the flow structure. The change of orientation of the averaged flow structure also occurs at $Ra = 3 \times 10^7$, 5×10^7 and 10^8. It has been observed that the flow in the range $3 \times 10^7 \leqslant Ra \leqslant 10^8$ evolves erratically between the different flow configurations and it was not possible to found a clear relation between the Rayleigh number and the time in which the flow maintains a certain configuration or the time needed by the flow to change between configurations.

The observed evolution of the flow between the different configurations in the range $3 \times 10^7 \leqslant Ra \leqslant 10^8$ implies different statistical properties of the time evolution of the different variables of the flow. Since these flow transitions occur at very low frequencies, the statistical properties of the variables that are sensitive to the particular

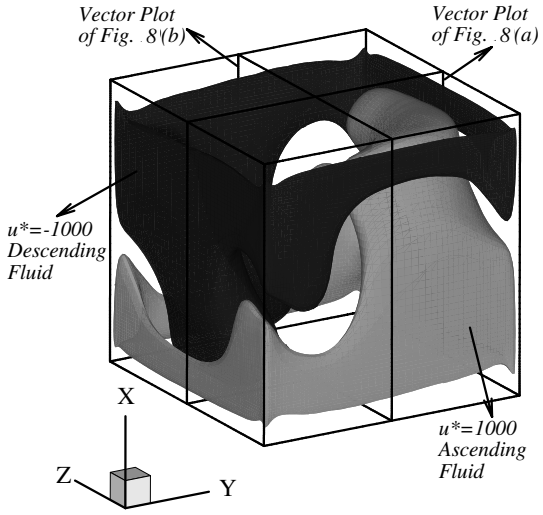

Fig. 7. Time averaged flow field at $Ra = 7 \times 10^7$ for the (C) configuration with a total integration time of $t_t^* = 0.16$ (156 min) in terms of the isosurfaces of the vertical velocity component, $u^* = \pm 1000$.

configuration of the flow are different from those that are more insensitive to the flow configuration. Table 4 shows that at the Rayleigh numbers in which the single roll is observed $(3 \times 10^7 \leqslant Ra \leqslant 10^8)$ the integral time scales of the vertical velocity and temperature on the horizontal mid plane of the cavity are drastically reduced in comparison with the evolutions of these variables at $Ra = 10^7$ because of the important contribution of the low frequencies associated with the transition between different flow configurations in their time evolutions. On the contrary the time evolution of other quantities, as the horizontal velocity component or the averaged Nusselt number which are not significantly affected by the evolution between configurations, show integral time scales of the same order of magnitude as those at $Ra = 10^7$. Table 4 shows that the increase of the RMS values as the Rayleigh is increased is more evident in the variables insensitive to the particular flow configuration than in the sensitive quantities. It is important to note that the influence of the low frequency evolution in the integral time scale of some specific flow quantities should be taken into account to determine adequate sampling periods for the calculation of the flow statistics.

The averaging procedure during the experiments at $Ra = 7 \times 10^7$ and at $Ra = 10^8$ was performed during 13 and 8 h, respectively. The time evolution of the vertical velocity at $x^* = 0.5$, $y^* = 0.75$ and $z^* = 0.5$ does not show low frequencies. However, the averaged flow structure of the vector field showed good agreement with the individual flow configuration obtained numerically (i.e. configurations (A), (B), (C) and (D)). This indicates that the time averaged flow structure experimentally obtained corresponds to only one of the flow configurations obtained numerically and consequently, it can be concluded that the transition between the configurations is not produced in the experiments.

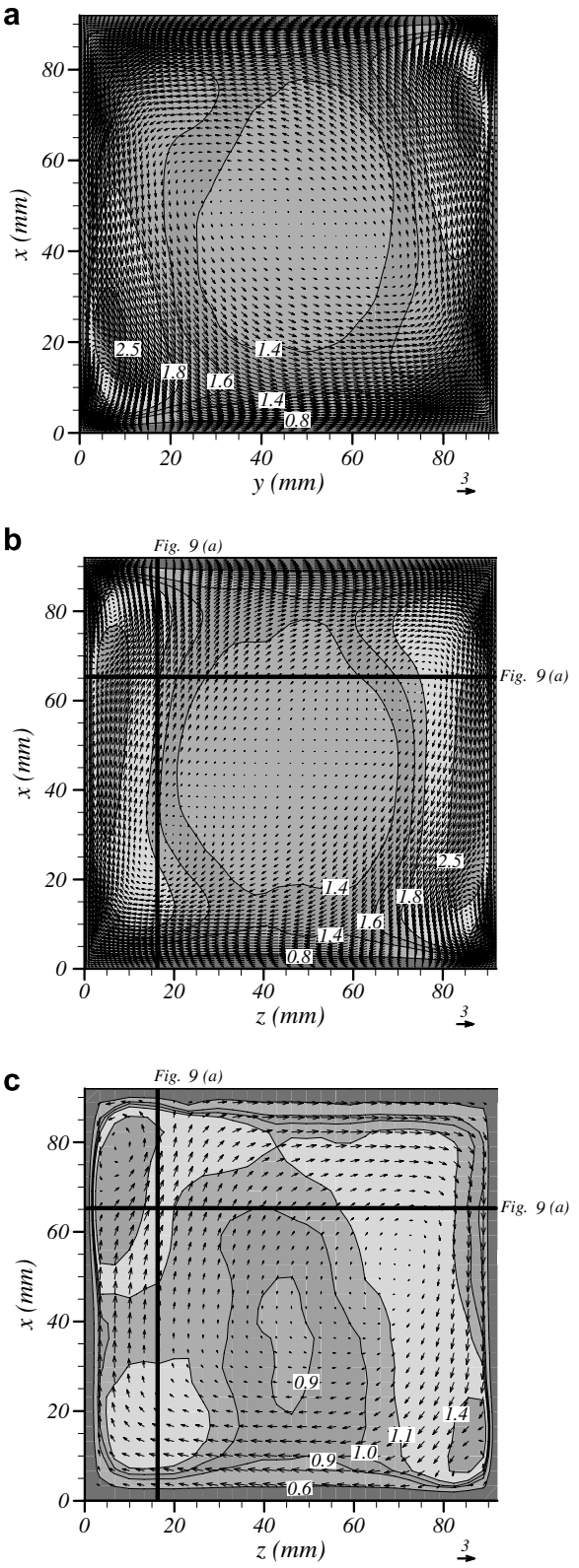

Fig. 8. Velocity fields and RMS values of u at $Ra = 7 \times 10^7$ on the vertical mid-planes. (a) and (b) numerical fields at $z = 46$ mm and $y = 46$ mm, respectively (c) experimental velocity field at $y = 46$ mm. These planes are indicated in Fig. 7. The reference vectors are depicted near the bottom right corner of each vector plot.

In order to check the influence of the horizontal inclination of the cavity, a simulation at $Ra = 7 \times 10^7$ was carried out with 0.1° of inclination in the y-direction and 0.2° in the z-direction. The time averaged flow structure obtained with this inclination was perfectly identified as the (D) configuration. In this case, the time evolution of the velocities did not show low frequencies and transition between flow configurations was not observed. This indicates that the relative stability of the configuration observed experimentally can be explained by the small horizontal misalignments of the experimental cavities that were estimated to be of the same order of magnitude than those introduced in this numerical simulation.

Because of the similitude of the time averaged flow structures found in the range $3 \times 10^7 \leqslant Ra \leqslant 10^8$, only the flow topologies at $Ra = 7 \times 10^7$ and $Ra = 10^8$ obtained numerically were validated with experiments. Although the averaging time during the experiments was 13/9 h at $Ra = 7 \times 10^7/Ra = 10^8$ only 3.5 h, 1.5 h, 2.6 h and 1.2 h/2.9 h, 3.9 h and 1.2 h were used for the configurations (A), (B), (C) and (D)/(A), (B) and (C), respectively, obtained numerically ($t_t^* = 0.22$, $t_t^* = 0.09$, $t_t^* = 0.16$ and $t_t^* = 0.08/t_t^* = 0.19$, $t_t^* = 0.25$ and $t_t^* = 0.08$, respectively).

Fig. 8 shows the velocity fields and the RMS values on the vertical mid-planes at $Ra = 7 \times 10^7$. In Fig. 8a and b the (C) configuration is plotted for the numerical simulations on the mid-planes $z^* = 0.5$ and $y^* = 0.5$, respectively. The corresponding measured velocity vector field on the mid-plane at $Ra = 7 \times 10^7$ is shown in Fig. 8c. It can be seen that there is a good qualitative agreement between the numerical and experimental velocity vectors and the RMS values of u, indicating that the experimental flow structure is well predicted by the numerical simulation. Fig. 9a shows the velocity profiles along the solid lines indicated in Fig. 8b and c for the (C) configuration. Note that the profiles corresponding to the other three configurations have been rotated accordingly to make the profiles comparable. Fig. 9b shows the velocity profiles at $Ra = 10^8$ along the same lines used at $Ra = 7 \times 10^7$ for the three configurations obtained at this Rayleigh number ((A), (B) and (C)). It can be seen that, in general, the measured velocities are within the numerically predicted velocity profiles for the different flow configurations.

The averaged flow structure obtained from the averaging of the different flow configurations at $Ra = 7 \times 10^7$ is shown in Fig. 10, in terms of isosurface of the second largest eigenvalue of the velocity gradient tensor [19] (Fig. 10a) and in terms of the velocity vectors field on a vertical mid-plane of the cavity ($z^* = 0.5$) (Fig. 10b). It can be seen that the averaging of the different orientations of the single roll, corresponding to the different flow configurations, produces the same overall two-ring flow topology observed at $Ra = 10^7$ (see Fig. 2a). This is consistent with the average flow structure that would be obtained by rotating, for example, the flow configuration shown in Fig. 8b, with respect to the vertical axis of the cavity.

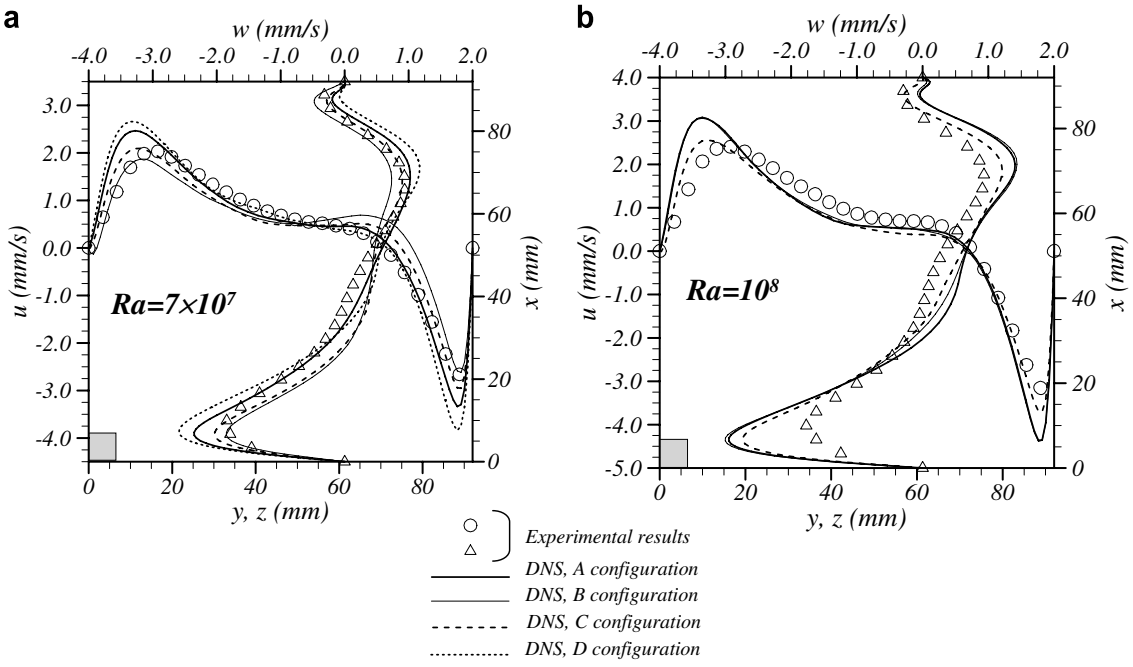

Fig. 9. Velocity profiles of the four possible configurations obtained numerically and measured experimentally. Vertical/horizontal profile of the horizontal/vertical velocity component (v/u) along the line $y = 16.5/x = 65.8$ mm, $y = 46$ mm ($y^* = 0.5$) (a) at $Ra = 7 \times 10^7$ and (b) at $Ra = 10^8$. The horizontal axis corresponds to y for the configurations A and B, and to z for the configurations C and D. The configuration D at $Ra = 7 \times 10^7$ had to be rotated in order to obtain comparable velocity profiles and the horizontal axis has to be read inversely, from 92 to 0 mm. The profiles at $Ra = 7 \times 10^7$ are indicated in Fig. 8a and b. The gray squares indicate the size of the interrogation window used in the experiments.

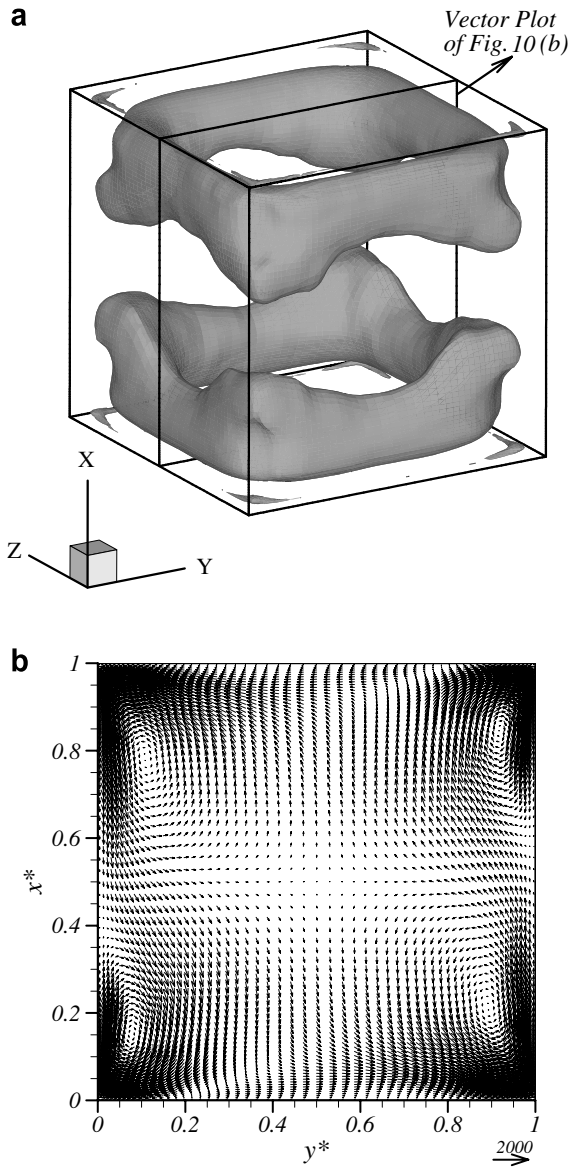

Fig. 10. Time averaged flow field calculated using four average data sets of approximately 3.7×10^5 time steps of each configuration ((A), (B), (C) and (D)) at $Ra = 7 \times 10^7$ (a) in terms of the isosurface of a constant value ($\lambda_2/|\lambda_{2,\max}| = -0.036$) of the second largest eigenvalue of the velocity gradient tensor and (b) in terms of the velocity field in the vertical mid-plane $z^* = 0.5$.

5. Concluding remarks

The time evolving and time average flow structures in the range $10^7 < Ra < 10^8$ were studied numerically and experimentally for water in a cubical enclosure heated from below with partially conducting lateral walls. The time averaged flow structure obtained at $Ra = 10^7$ consisted in two main counter rotating vortex rings parallel to the horizontal walls. In the range $3 \times 10^7 < Ra < 10^8$ the flow was characterized by a single rolling motion with ascending and descending currents located close to two diagonally opposed vertical edges. The time evolution of the vertical velocity component in one point of the cavity in this range of Rayleigh numbers shows low frequencies that correspond to the progressive rotation of this single roll motion around the vertical axis of the cavity. For the Rayleigh studied here, it was not possible to found a clear relation between the Rayleigh number and the time in which the flow maintains a certain configuration or the time needed by the flow to change between configurations. The time averaged flow topologies numerically predicted were also observed experimentally using the PIV technique at $Ra = 10^7$. At $Ra = 7 \times 10^7$ and $Ra = 10^8$ the rotation of the orientation of the single roll obtained numerically was not observed, probably because of the extreme sensitivity of this rotation to the horizontal misalignments of the cavity, as suggested by numerical simulations of the flow in cavities with small inclinations. The differences of the averaged heat transfer rates and the overall flow structure between partially conducting walls and perfectly conducting lateral walls at $Ra = 10^7$ are not significant but differences in velocities can reach 110% indicating that the experimental results are better predicted when a finite thermal conductivity is considered in the calculations. Finally, this study shows that the numerical prediction of Rayleigh–Bénard convection in a cubical cavity at intermediate Rayleigh numbers is an excellent benchmark problem for the study of transitional flows.

Acknowledgement

This study was financially supported by the Spanish Ministry of Science and Technology under projects DPI2003-06725-C02-01 and VEM2003-20048.

References

[1] H. Ozoe, K. Yamamoto, S.W. Churchill, H. Sayama, Three-dimensional, numerical analysis of laminar natural convection in a confined fluid heated from below, J. Heat Transfer 98 (1977) 202–207.
[2] R. Hernández, R.L. Frederick, Spatial and thermal features of three dimensional Rayleigh–Bénard convection, Int. J. Heat Mass Transfer 37 (3) (1994) 411–424.
[3] J. Pallares, I. Cuesta, F.X. Grau, F. Giralt, Natural convection in a cubical cavity heated from below at low Rayleigh numbers, Int. J. Heat Mass Transfer 39 (15) (1996) 3233–3247.
[4] J. Pallares, I. Cuesta, F.X. Grau, Laminar and turbulent Rayleigh–Bénard convection in a perfectly conducting cubical cavity, Int. J. Heat Fluid Flow 23 (2002) 346–358.
[5] L. Valencia, J. Pallares, I. Cuesta, F.X. Grau, Rayleigh–Bénard convection of water in a perfectly conducting cubical cavity: effects of temperature – dependent physical properties in laminar and turbulent regimes, Numer. Heat Transfer, Part A: Appl. 47 (5) (2005) 333–352.
[6] D.D. Gray, A. Giorgini, The validity of the Boussinesq approximation for liquids and gasses, Int. J. Heat Mass Transfer 19 (1976) 545–551.
[7] W.H. Leong, K.G.T. Hollands, A.P. Brunger, Experimental Nusselt numbers for a cubical-cavity benchmark problem in natural convection, Int. J. Heat Mass Transfer 42 (11) (1999) 1979–1989.
[8] D.M. Kim, R. Viskanta, Study of the effects of wall conductance on natural convection in differently oriented square cavities, J. Fluid Mech. 144 (1984) 153–176.
[9] J. Salat, S. Xin, P. Joubert, A. Sergent, F. Penot, P. LeQuéré, Experimental and numerical investigation of turbulent natural

convection in a large air-filled cavity, Int. J. Heat Fluid Flow 25 (2004) 824–832.
[10] G. Ahlers, Effect of sidewall conductance on heat-transport measurements for turbulent Rayleigh–Bénard convection, Phys. Rev. E 63 (2000) 015303/1-4.
[11] R. Verzicco, Sidewall finite-conductivity effects in confined turbulent thermal convection, J. Fluid Mech. 473 (2002) 201–210.
[12] M.P. Arroyo, J.M. Savirón, Rayleigh–Bénard convection in a small box: spatial features and thermal dependence of the velocity field, J. Fluid Mech. 235 (1992) 325–348.
[13] M. Raffel, C. Willert, J. Kompenhans, Particle Image Velocimetry, first ed., Springer, Berlin, 1998.
[14] L. Valencia, Estudio numérico y experimental del flujo Rayleigh–Bénard en cavidades cúbicas para régimen transitorio y turbulento, Ph.D. thesis, Universitat Rovira i Virgili, Tarragona, Spain, 2005.
[15] F.P. Incropera, D.P. DeWitt, Fundamentos de Transferencia de Calor, fourth ed., Pearson–Prentice Hall, Mexico, 1996, pp. 846–847.
[16] M.C. Potter, D.C. Wiggert, Mecánica de Fluidos, second ed., Prentice-Hall, México, 1997, pp. 754.
[17] J.P. Holman, Heat Transfer, fourth ed., Mc Graw-Hill Kogakusha Ltd., Tokyo, 1976, pp. 253, 499, 507.
[18] I. Cuesta, Estudi Numéric de Fluxos Laminars i Turbulents en una Cavitat Cúbica, Ph.D. thesis, Universitat Rovira i Virgili, Tarragona, Spain, 1993.
[19] J. Jeong, F. Hussain, On the identification of a vortex, J. Fluid Mech. 285 (1995) 69–80.
[20] B. Lecordier, D. Demare, L.M.J. Vervisch, J. Réveillon, M. Trinité, Estimation of the accuracy of PIV treatments for turbulent flow studies by direct numerical simulation of multi-phase flow, Measur. Sci. Technol. 12 (2001) 1382–1391.